Aerodynamic and acoustic analysis of an optimized low Reynolds number rotor

Ronan Serré[1]*, Nicolas Gourdain[1], Thierry Jardin[1], Adrián Sabaté López[1], Viswesh Sujjur Balaramraja[1], Sylvain Belliot[1], Marc C. Jacob[1], Jean-Marc Moschetta[1]

ISROMAC 2017

International Symposium on Transport Phenomena and Dynamics of Rotating Machinery

Maui, Hawaii

December 16-21, 2017

Abstract

The demand in Micro–Air Vehicles (MAV) is increasing as well as their potential missions. Either for discretion in military operations or noise pollution in civilian use, noise reduction of MAV is a goal to achieve. Aeroacoustic research has long been focusing on full scale rotorcrafts. At MAV scales however, the hierarchization of the numerous sources of noise is not straightforward, as a consequence of the relatively low Reynolds number that ranges typically from 5,000 to 100,000. This knowledge however, is crucial for aeroacoustic optimization. This contribution briefly describes a low–cost, numerical methodology to achieve noise reduction by optimization of MAV rotor blade geometry. That methodology is applied to reduce noise from a MAV developped at ISAE–Supaero and a 8 dB(A) reduction on the acoustic power is found experimentally. The innovative rotor blade geometry allowing this noise reduction is then analyzed in detail using high–fidelity numerical approaches such as Unsteady Reynolds Averaged Navier–Stokes (URANS) simulation and Very Large Eddy Simulation using Lattice Boltzmann Method (VLES–LBM). That strategy gives insight into the flow features around the optimized rotor and guidelines for the acoustic models used in a low–cost numerical optimization loop.

Keywords

Aeroacoustics — Low noise optimization — Micro–Air Vehicles

[1] *Department of Aerodynamics, Energetics and Propulsion (DAEP), ISAE–Supaero, Toulouse, France*

*__Corresponding author__: ronan.serre@isae.fr

INTRODUCTION

Designing a silent rotor goes through an aeroacoustic optimization, which implies understanding the aerodynamic phenomena responsible for noise generation. Predicting the noise generated aerodynamically is relatively straightforward once detailed aerodynamics involved in the propulsion system are available through the use of direct noise computation or hybrid prediction. Aeroacoustic optimization in that framework is possible [1, 2] but demanding in terms of computational cost hence not realistic in an industrial context. To this aim, lower–fidelity tools are needed. The numerical tool discussed in the present paper is suited for engineering purposes. It contains an aerodynamic model, acoustic models for tonal and broadband noise and optimization algorithms. A similar strategy has been followed by Wisniewsky *et al.* [3] and Zawodny *et al.* [4] with models based on empirical data at relatively high Reynolds numbers and for symetrical profile. The present study proposes a more general methodology. The optimization consists in a systematic scanning of the parameters space defined by chord and twist laws as a function of the blade radius and rotor rotation speed with constant thrust as objective. The blade chord and twist laws are parameterized by Bézier curves considering control points in 4 sections along the blade span giving 8 variables. However, in order to ensure that lift at blade tip vanishes, which is required to minimize induced velocity, the twist at the fourth control point is set to zero eventually giving 7 variables. In the combination method, each variable can take 4 values giving 4^7 individual evaluations. A multi–objective selection is applied to express the pareto front according to lower power consumption and lower overall sound pressure level. The numerical tool allows airfoil section optimization although this paper focuses on investigating one optimized geometry previously obtained. The effect of the airfoil section optimization has been addressed in a companion paper [5] and will not be discussed hereafter. For each set of parameters, the blade loading is obtained using Blade Element and Momentum Theory (BEMT) as described by Winarto [6]. Distributions of lift and drag and global thrust and torque are retrieved from local lift and drag coefficients of the blade element airfoil sections. Knowledge of the aerodynamic polar of the considered airfoil section is essential. Three strategies may be employed to this end: experimental [7], high–fidelity simulation [8] or low–fidelity modeling [9]. The last one is used in the present study for effectiveness. Lift and drag coefficients are extracted from Xfoil open–source software by Drela [9], as well as boundary layer data. That software is based on potential theory with viscosity models. It was shown in a previous paper [5] that Xfoil provides results in agreement with experiments. For that reason, it is used herein to provide input data to the optimization tool. The aerodynamic model based on BEMT is fast and reliable but yields a steady loading on the blades and that reduces *a priori* the ability to predict noise radiation, for acoustics is intrinsically unsteady. However, because of the relative motion between the spinning blades and a static observer, acoustic radiation can still be retrieved

from a steady loading but only the main tonal part from the periodic excitation. Having access to unsteady aerodynamics would enhance model predictions but dramatically increases computational cost in the optimization process. The acoustic spectrum radiated by rotors exhibits also a broadband part [10]. Low–fidelity broadband models are added in the optimization process to enrich the acoustic prediction. The acoustic modeling is performed in two steps: *i)* an integral method based on the Ffowcs Williams and Hawkings [11] (FWH) equation gives the tonal noise radiated by the rotor from the steady loading yielded by the BEMT and *ii)* analytical models estimate the broadband part of the acoustic spectrum based on the work of Roger and Moreau [12]. The FWH equation is implemented in the time domain in the form known as Formulation 1A [13] and applied on the blade surface. The quadrupole term is removed from the FWH equation and since the integration surfaces correspond to the blades, no quadrupole source is taken into account. This is physically consistent with the low Mach number context of the MAV rotors [14]. As a consequence, the FWH reduces to thickness and loading noise computation obtained from the two surface integrals. The main input parameters are the incoming flow velocity at the blade element influencing the thickness noise and the force distributions acting on the loading noise. In that steady loading framework, the latter is found to be relatively small without significantly contributing to the overall noise while the former is found to be dominant independently of the observer's location. In addition, three sources of broadband noise are considered: the scattering of boundary layer disturbances as sound by the trailing edge, the ingestion of turbulence at the leading edge and the shedding of vortical eddies in the wake [12]. The first two models are active in the optimization tool after being calibrated with materials presented in this paper. The third model is left for future work. The main inputs for the trailing edge noise model are the wall pressure spectrum and the spanwise coherent length and both can be modelled from boundary layer data. Boundary layer information is accessible from Xfoil software and thus, the trailing edge noise model is the most straightforward. The main input for the turbulence interaction noise model is turbulence statistics. It was then decided to run a first optimization with the sole trailing edge noise model and to investigate the optimized geometry with higher fidelity simulations to have access to such turbulence statistics that could help calibrate the turbulence interaction noise model. The broadband noise models are implemented according to the formulations proposed by reference [12], a slight correction that accounts for low–aspect ratio wings from the strip theory framework notwithstanding. The broadband noise models are then modified by a Doppler shift imposed by the relative motion between the source and the observer and integrated over a rotation cycle [15]. During the optimization process, only one observer location is considered, located 45° above the rotor plane, 1 m away from the center of rotation.

1. OPTIMIZATION RESULTS AND MEASUREMENTS

The optimization tool is used at ISAE–Supaero to determine a low noise MAV blade geometry. Chord and twist distribution laws were derived from a range of possibilities in the spanwise chord–twist space for several numbers of blades per rotor at constant thrust of 2.85 N required for hovering flight, allowing for rotational speed to adjust. The airfoil section is a thin, cambered Goëttingen 265, suitable for low Reynolds number flow. The conventional rotor compared to the optimized configurations is a two–blade commercial rotor with APC7x5 blades, mounted on the ISAE–Supaero MAV. Since the airfoil section of APC7x5 blades was unknown to the authors, the conventional rotor and the best optimized one are compared experimentally. The optimized rotors are manufactured using SLA technology on a $3D$ printer with a 50 μm vertical resolution. The measurements take place in

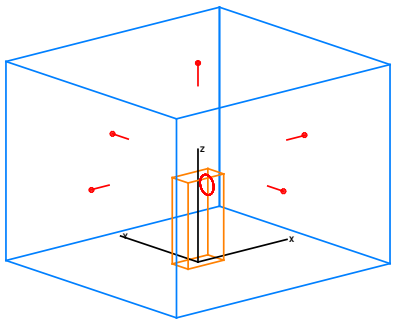

Figure 1. Schematic view of the experimental set–up following the ISO 3746 : 1995 standard. The source (orange) is surrounded by the measurement surface (blue) on which the microphones are positionned (red). The axis are indicated in black and represent unit length. The plane of rotation is represented by the red circle.

a rectangular room, not acoustically treated of dimensions $(l_1 \times l_2 \times l_3) = (14.9 \times 4.5 \times 1.8)$ m^3. The aerodynamic forces are retrieved from a five components balance. To ensure the validity of sound measurements in a room that is not acoustically treated, the sound power level is computed according to ISO 3746 : 1995 standard with five measurement points 1 m around the rotor as illustrated in figure 1, on a Brüel & Kjær 1/2″ free–field microphone and a Nexus frequency analyzer with a frequency resolution of 3.125 Hz. The microphones are in the acoustic far–field, the distance between the source and the microphones approximately representing 5 rotor diameters. Four of the microphones are on a meridian line parallel to the ground and centered on the axis of rotation and a fifth microphone is located in the plane of rotation. The maximum noise reduction for the optimized geometries is achieved by the three–bladed configuration according to measurements. Its chord and twist distribution laws are plotted in figure 2 with those of the conventional rotor. The radial position is normalized by the tip radius

$R = 0.0875$ m. The twist angle is defined with respect to the plane of rotation. The optimized chord is larger and the twist laws are approximately the same, except at 75% of blade span where the optimized twist increases again before vanishing at the tip. Comparisons between the aerodynamic performance

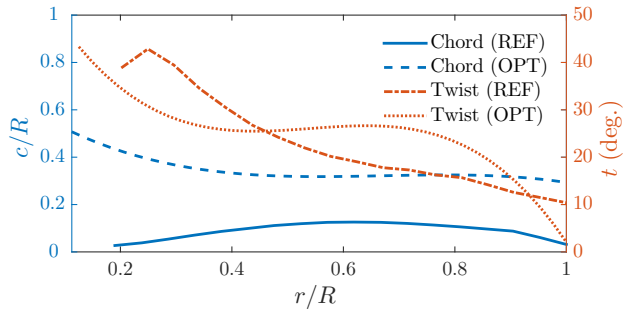

Figure 2. Chord and twist distribution laws for the conventional rotor ("REF") and the optimized rotor ("OPT"). Normalized by tip radius $R = 0.0875$ m.

of the conventional rotor and the three–blade optimization are shown in figure 3 for the thrust coefficient and in figure 4 for the figure of merit at several rotational speeds. The thrust coefficient and the figure of merit, respectively C_t and FM are defined according to reference [16] as

$$C_t = \frac{T}{\frac{1}{2}\rho(\omega R)^2 \pi R^2} \; ; \; FM = \frac{T^{3/2}}{\omega Q \sqrt{2\rho\pi R^2}} \tag{1}$$

where T is the thrust, Q is the torque, ρ is the ambient density, ω is the rotational frequency and R is the rotor tip radius. The thrust objective is reached at approximately 5,400 rpm *versus* 8,500 rpm for the conventional rotor (figure 3). The figure of merit is higher for the optimized rotor than for the conventional one (figure 4) although it is decreasing with the rotational speed for the optimized rotor while increasing for the conventional rotor. When the thrust objective is reached the optimized rotor has a figure of merit 1.3 times higher that the conventional rotor whereas the thrust coefficient is 3 times higher (figure 3). This indicates that the optimized rotor is aerodynamically more efficient. The figure of merit might however be overestimated for the aerodynamic balance used in the experiment underestimates the torque. A reduction of 8 dB(A) in the acoustic power is observed between the conventional rotor and the optimized one at the thrust objective (figure 5). At same rotational speed however, the optimized rotor radiates more acoustic energy. The measurements are carried out in a regular room without acoustic treatments and influenced by ambient noise thus explaining the observed standard deviation. At 4,500 rpm, the standard deviation is particularly high for the optimized rotor which might indicate the triggering of a separation phenomenon as will be discussed in the next section. From typical spectra measured for both rotors (figure 6), it can be concluded that sound power reduction is a consequence of noise reduction in both tonal and broadband parts of the acoustic spectrum.

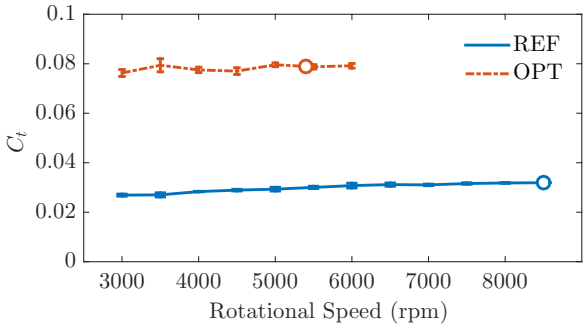

Figure 3. Thrust coefficient. Conventional rotor ("REF") and optimized rotor ("OPT"). Blank symbols indicate value at thrust objective. Measurements with standard deviation.

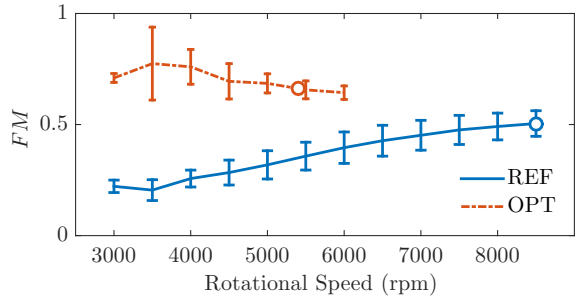

Figure 4. Figure of merit. Conventional rotor ("REF") and optimized rotor ("OPT"). Blank symbols indicate value at thrust objective. Measurements with standard deviation.

The mid frequency harmonics (between 2,000 and 6,000 Hz) have been significantly reduced and even removed in some cases as can be seen in the picture inserted in figure 6. Such a feature might have positive impact on the perception of noise reduction under psycho–acoustic considerations [17]. It is difficult to identify a specific noise source mechanism in the measured acoustic spectrum for several reasons: *i)* the noise produced by the motor itself has not been isolated and its rotational speed is fluctuating, creating additional noise; *ii)* the inflow has not been characterized, it is then unkown if distortion effects are to be expected; *iii)* the measurement procedure allows to compute acoustic power from non–anechoic environment but a single acoustic pressure spectrum still includes reflections and external noise. Moreover, the experimental test bench holds the rotor in such a way that its axis of rotation is parallel to the ground. As a consequence, a stand that includes the aerodynamic balance is mounted vertically, behind the rotor, eventually yielding unsteady loading on the blades creating more additional noise radiation at the blade passing frequencies. Nevertheless, the followed procedure aimes at identifying a relative noise reduction by evaluating every rotor in the same conditions. The optimization tool has proven its effectiveness to propose an innovative geometry achieving noise reduction while increasing endurance. The three–blade optimization is used as a reference for detailed investigations. As mentionned

in the introduction, at this early stage of development the optimized rotor was obtained with only the trailing edge noise model active in the optimization tool. It is expected that optimizations can be enhanced by taking into account other broadband noise sources and by investigating the aerodynamic flow features around the optimized geometry. A higher level of noise reduction is expected.

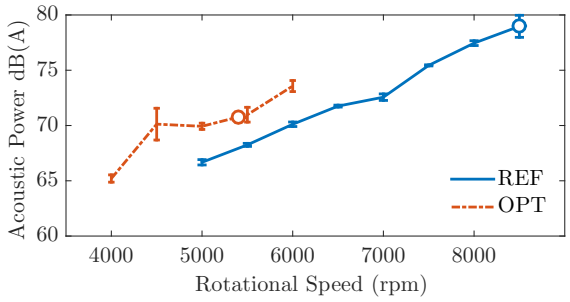

Figure 5. Acoustic power. Conventional rotor ("REF") and optimized rotor ("OPT"). Blank symbols indicate value at thrust objective. Measurements with standard deviation.

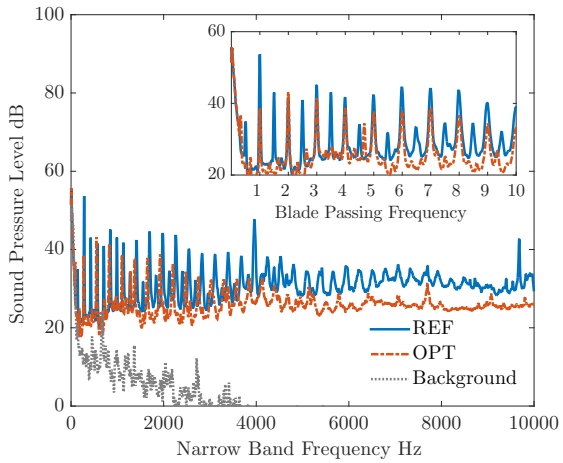

Figure 6. Acoustic spectra for the conventional rotor ("REF") and the optimized rotor ("OPT") at the rotational speed of the thrust objective. The spectra are averaged over microphone positions and measurement sessions. Close–up view with frequencies normalized by the blade passing frequency.

2. AERODYNAMIC INVESTIGATION FROM HIGH FIDELITY METHODS

Two additional numerical strategies are used to analyze the aerodynamic and the acoustic characteristics of the optimized rotor. Note that these two strategies simulated only the rotor without installations. A first strategy is based on the Lattice–Boltzmann Method, referred to as LBM, and is used to perform a Large–Eddy Simulation. Beyond computational performance, the main advantage of LBM is that the method is stable without artificial dissipation, which makes it equivalent to solve the Navier–Stokes equations with a high–order numerical scheme [18]. The present discretization of the equations ensures that the method is second–order accurate both in time and space. The LBM equations are solved using the open source software Palabos (`www.Palabos.org`) on a cubic domain with an edge of about $45R$. The mesh of the rotor is composed of 249 million Cartesian cells. Boundary conditions are coupled with a buffer layer of 1 m to avoid spurious reflections. The dimension of the first cell layer at the rotor wall is 350 μm to obtain an $y+$ of 50 in the tip region. One rotor revolution is achieved in 250 time steps and data are extracted after 8 revolutions. A second strategy resolves the three–dimensional incompressible Reynolds–Averaged Navier–Stokes (URANS) equations on a cylindrical domain of diameter $20R$ and length $50R$ enclosing the rotor. Numerical resolution is achieved using a finite volume approach by means of StarCCM+ commercial code. The computational domain is discretized using 8 million polyhedral cells with a typical size in the vicinity of the rotor of $R/176$. The boundary conditions upstream and downstream the rotor are implemented as pressure conditions while the periphery of the domain is treated as a slip wall. The blades are modelled as no–slip surfaces. A full rotation is dicretized into 360 time steps and at least 35 rotations are needed to ensure that initial transients have sufficiently decayed. Both spatial and temporal discretizations are achieved using second order schemes. Finally, the k–ϵ model is employed for URANS turbulence closure with maximum $y+$ values below unity. Note that Spalart–Allmaras and k–ω SST models (with and without gamma–Re–theta transition model) were tested and yielded similar results to those obtained using the k–ϵ model in terms of integrated loads. In addition, it was verified that the results are converged with respect to the typical cell size. Analyzing the characteristics of the optimized geometry with high–fidelity numerical simulations serves three objectives: *i)* validate the aerodynamic model in the optimization tool, *ii)* calibrate and validate the acoustic broadband models and *iii)* rank the noise sources in MAV rotors. Analyzing the LBM simulation also provides informations on the flow features around the optimized rotor and helps identify specific characteristics such as stall phenomena or leading edge separation as can be seen in figure 7. Such a phenomenon occurs around 75% of the blade radius, where the twist angle increases again (figure 2) suggesting that having an inflection point on the twist distribution law should be avoided. The resulting flow then merges with the tip vortex and impinges the following blade. It creates an interaction noise that is believed by the authors to be the most dominant noise source in this configuration.

2.1 Validation of the aerodynamic model

The rotational speed in U–RANS and LBM simulations was set at 5,000 rpm as was predicted by BEMT to reach the thrust objective. It was observed in the experiment to be underestimated as the actual rotation speed needed to reach the thrust objective is around 5,400 rpm. An additional computation

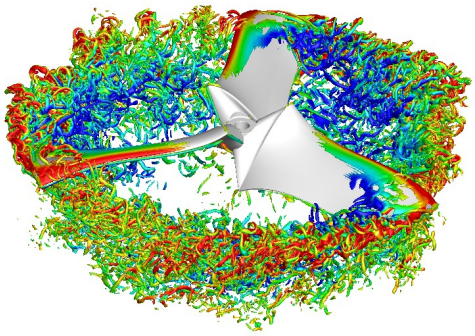

Figure 7. Iso–surface of Q–criterion colored by longitudinal velocity for the optimized rotor at 5,000 rpm. LBM simulation.

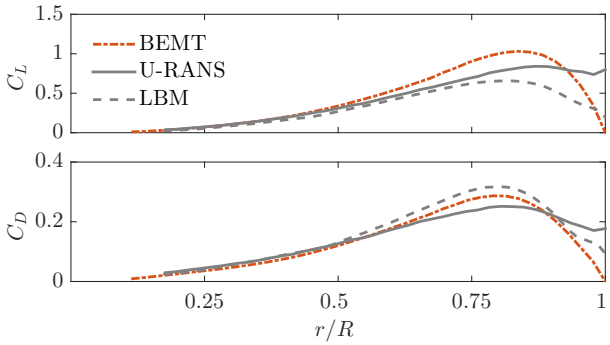

Figure 8. Forces distributions along the span of the optimized geometry at 5,000 rpm. Predictions from the aerodynamic model of the numerical tool (BEMT), URANS and LBM numerical simulations.

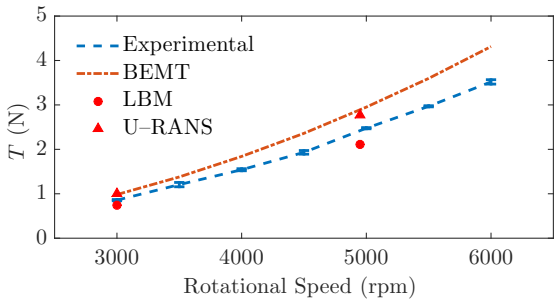

Figure 9. Thrust. Measurements with standard deviation and numerical predictions from the aerodynamic model of the optimization tool (BEMT), URANS and LBM numerical simulations. Optimized geometry.

was performed at 3,000 rpm. The lift and drag coefficients, respectively C_L and C_D, are depicted in figure 8 for the three numerical strategies along the span of the optimized blade at 5,000 rpm. The radial discretization is about 2%. The lift is slightly overestimated by the optimization tool leading to a lower rotational speed for the thrust objective. The drag however is well predicted. The BEMT model predicts a zero lift at tip because of the twist angle that is set to zero but numerical simulations exhibit a higher value in that region where vortex activity is strong. The three numerical strategies are in agreement up to 60% of the tip radius where separation phenomena begin to occur. The global performance are depicted in figures 9 and 10 for the thrust and the torque respectively. BEMT model and URANS simulation overestimate thrust as a consequence of the lift overestimation seen in figure 8. The torque is overestimated for every numerical strategies even though URANS prediction on the drag coefficient was lower than the other strategies. The BEMT prediction is the closest to the experimental data. It is however reminded that the aerodynamic balance used in the experiment underestimates the torque. A noteworthy source of discrepancy between measurements and numerical predictions is the surface quality of the printed rotors for it has to be sanded and that drives the behavior of the boundary layer.

2.2 Calibration of broadband noise models

As previously outlined, only the trailing edge noise model was activated during the optimization process. The other two models needed further calibration and validation. The broadband models available for the optimization tool mainly require three main input parameters: the wall pressure fluctuation spectrum ϕ_{pp} associated with the spanwise correlation length in the frequency domain for the trailing edge noise model and the cross–correlated upwash velocity fluctuation spectrum ϕ_{ww} in the wavenumber space [19] for the turbulence ingestion and the vortex shedding noise models. The spanwise correlation length is approximated using Corcos model [12] with highpass filtering. Other models as discussed in reference [20] were investigated but were found to lack robustness without suitable boundary layer data. In order to estimate ϕ_{pp}, several models are available in the literature with a review provided by Blandeau [21] and are compared to the wall pressure fluctuation spectrum measured from the LBM simulation at the trailing edge of the optimized blade (figure 11). The main parameters for these models are boundary layer informations estimated in the present study from the Xfoil software [5]. The model from Kim and George [22] is included in the optimization tool for it gives less deviation than the other models and is the only one based on airfoils experiments instead of flat plates. It is expected to yield an underestimated trailing edge noise at low frequencies and a slightly overestimated noise at high frequencies. As will be discussed, trailing edge noise is found to be relatively weak. Moreover, if the models are known to overestimate high frequencies, trailing edge noise might not be a dominant source of noise in MAV rotors. However, because of the lack of large time sampling used in the LBM simulation, low frequencies should not be regarded as relevant. For the other two broadband models, information on impinging turbulence is required through the cross–correlated upwash velocity fluctuation spectrum ϕ_{ww}. The models proposed by von Kármán

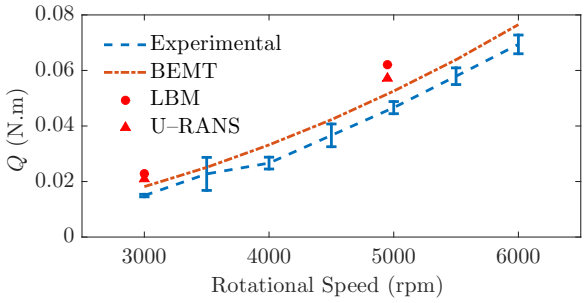

Figure 10. Torque. Measurements with standard deviation and numerical predictions from the aerodynamic model of the optimization tool (BEMT), URANS and LBM numerical simulations. Optimized geometry.

and Liepmann cited in reference [23] are compared to data from the LBM simulation just upstream of the leading edge of one blade in the optimized rotor as shown in figure 12 for $k_x = \omega/U_0$, U_0 being the uniform convection velocity under the frozen–turbulence assumption and $k_y = 0$. The modeling of ϕ_{ww} is expected to yield the right trend although it overestimates the whole spectrum. It is worth noting that the order of magnitude in the error of the estimated ϕ_{pp} or ϕ_{ww} also impacts the overall sound pressure level. That is to say, if the fluctuation spectrum models are estimated 10 times higher than the effective value, the overall sound pressure level is 10 dB higher. The von Kármán and Liepmann models depend on the wavenumbers and two scales representative of the turbulence impinging the leading edge which in turn causes interaction noise. These two scales are the intensity of the chordwise velocity fluctuation and the Taylor micro–scale L_μ as the turbulence length scale. That turbulence length scale can be directly derived from the LBM simulation and is depicted in figure 13. The turbulence appears to be relatively homogeneous both in the vertical direction (z/R) and in the radial direction (r/R) between 60% and 90% of the blade radius. It is however necessary to approximate this quantity

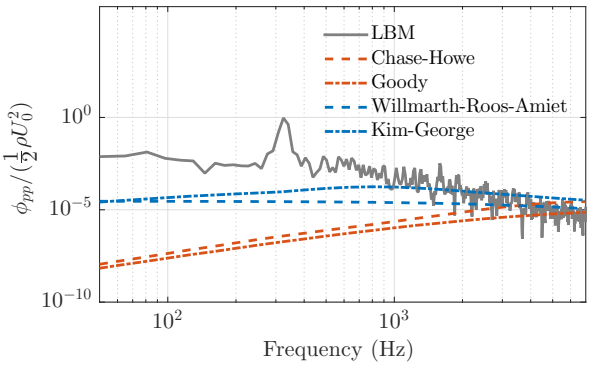

Figure 11. Wall pressure fluctuation spectrum ϕ_{pp} at the trailing edge, mid–span of the optimized blade from LBM simulations and numerical models.

with data already available in the optimization tool. In the

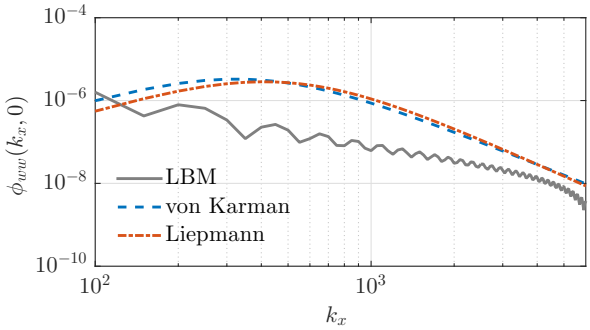

Figure 12. Cross–correlated upwash velocity fluctuation spectrum ϕ_{ww} upstream of the leading edge of the optimized blade from LBM simulations and numerical models.

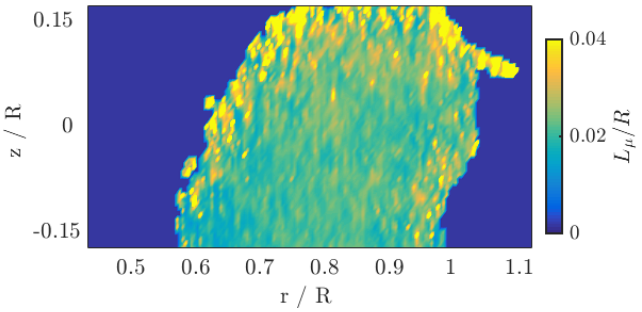

Figure 13. Taylor micro–scale L_μ upstream of the leading edge of the optimized rotor normalized by maximum radius. LBM simulation.

context of a clean inflow condition, the turbulence impinging the leading edge is believed to be generated by the wake of the trailing edge of the previous blade as it is believed to be stalled in this context. A similitude is then expected to be found between leading edge turbulence and trailing edge wake. The boundary layer informations from Xfoil are used to estimate the width of the wake near 90% of the chord according to the definition proposed in reference [24]:

$$D_w^* = d_{AS} + \delta_p^* + \delta_s^* \tag{2}$$

where d_{AS} is the airfoil section thickness near the trailing edge and δ_p^* and δ_s^* are the boundary layer displacement thicknesses on pressure side and suction side respectively. A comparison between the turbulence length scale measured from the LBM simulation upstream of the leading edge and an estimate of the wake width from the numerical tool is plotted in figure 14. It is unknown whether that scaling is relevant in every situations before further investigations are carried out but helpful equivalence is observed. For the following optimizations, the turbulence length scale is estimated from the Xfoil software based on boundary layer data and equation (2) to feed the ϕ_{ww} models. A way to scale the intensity of the chordwise velocity fluctuation is still under investigation. For the following computations, a value of 4 m/s is taken from LBM simulation, representing 10% of the tip speed.

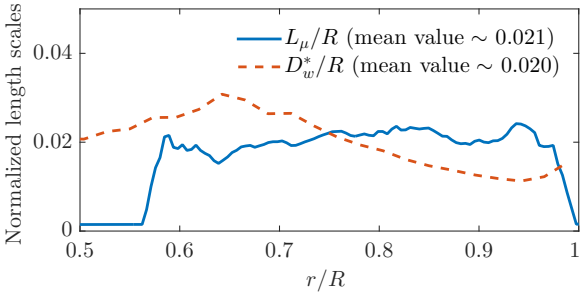

Figure 14. Comparison of length scales representative of turbulence and wake. L_μ predicted from LBM simulation and D_w^* predicted from the optimization tool. Normalized by tip radius.

3. AEROACOUSTIC INVESTIGATION FROM HIGH FIDELITY METHODS

An aeroacoustic solver is developped to predict the noise from the LBM simulation. It solves the FWH equation in the frequency domain [25] on a cartesian, permeable control surface surrounding the optimized rotor. The permeable control surface is centered on the rotor and is two rotor diameters long in the directions parallel to the rotor plane (axis $e_{\vec{x}}$ and $e_{\vec{y}}$) and one rotor diameter long in the direction parallel to the axis of rotation (axis $e_{\vec{z}}$). Aerodynamic data are extracted for three rotor revolutions with a relatively high frequency resolution ($\sim$ 30 Hz). The purpose is first to assess the ability of LBM simulation to provide valuable information for wave propagation methods [26]. It is believed that LBM simulation is a natural candidate for providing aerodynamic input to aeroacoustic analogies if care is taken to ensure that eddies do not cross the control surfaces. Although a promising filtering procedure has been recently proposed in reference [27] to suppress spurious signal from permeable FWH solver, it does not appear mature. A weighting coefficient is applied on the multipole definitions as suggested by Lockard [28]. The acoustic prediction resulting from the LBM simulation is compared to the optimization tool predictions and measurements on the acoustic power computed according to ISO 3746 : 1995 standard. Computations are run with the optimization tool for two configurations: with the trailing edge noise model only (labelled "TE") and in addition with the turbulence interaction noise model (labelled "TE+TI"). Results are shown in figure 15. Figure 15 indicates that turbulence interaction noise is dominant compared to trailing edge noise and this may be a consequence of the large coherent structures shed into the wake as observed in figure 7 that impinge the following leading edge causing the interaction noise. The computations are now systematically carried out with the interaction noise model in addition to the trailing edge noise model. The acoustic powers at a rotational speed of 5,000 rpm are reported in table 1. The corresponding sound power levels are plotted in figure 16 in third octave centered frequency bands according to ISO 3746 : 1995 standard. The prediction from the optimization tool is in relative agreement with the measurements while the prediction from the LBM simulation is higher. The power level of the BPF and subharmonics observed in the measurement are higher than those predicted by the optimization tool and that is a consequence of installation effects and unsteady loading. Figure 16 shows that most of the frequencies are overpredicted by the FWH solver and that overestimation is found again on the acoustic power (table 1). As previously mentionned, sound is propagated from aerodynamic data stored for three rotor revolutions: this relatively large sampling might be the cause of the observed discrepancy. It is worth noting that turbulent eddies crossing the permeable control surfaces might also be responsible for creating spurious noise [27]. Acoustic propagation is extracted from the LBM simulation and compared

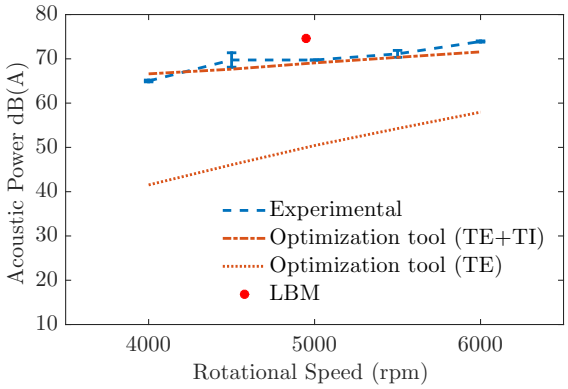

Figure 15. Acoustic power from measurements with standard deviation and numerical predictions from the optimization tool and LBM simulation.

Table 1. Acoustic power for the optimized rotor at 5,000 rpm according to ISO 3746 : 1995 standard.

Experimental	69.7 dB(A)
Optimization tool	69.1 dB(A)
FWH-LBM	73.9 dB(A)

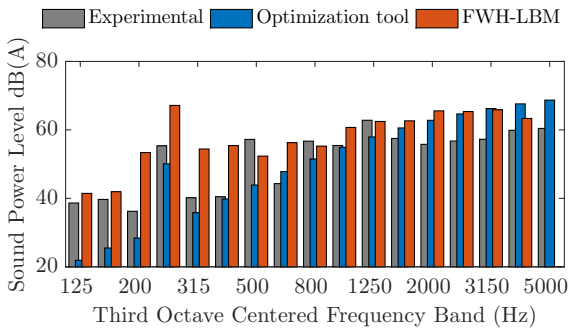

Figure 16. Acoustic power spectra according to ISO 3746 : 1995 standard between measurements, numerical prediction from the optimization tool and FWH propagation of LBM simulation.

with the predictions from the FWH–LBM tool. That overestimation of the blade passing frequency is observed on the acoustic power spectral density (PSD) plotted in figure 17 both from the FWH–LBM tool and the direct measurements of the LBM simulation. The signals are taken in the rotor plane, corresponding with one microphone position, approximately 1 m away from the rotor. Numerical predictions observed in figure 17 are a preliminary result: the PSD seems higher for every frequency than the measurements and that might be a consequence of the large frequency resolution available from the LBM simulations. The BPF is particularly overestimated. The FWH–LBM tool proves its relevance at higher frequencies. In this domain, mesh discretization of the LBM simulation reaches the same order of magnitude than the acoustic wavelength and a significant dissipation occurs. The FWH solver is a numerical tool that can be used

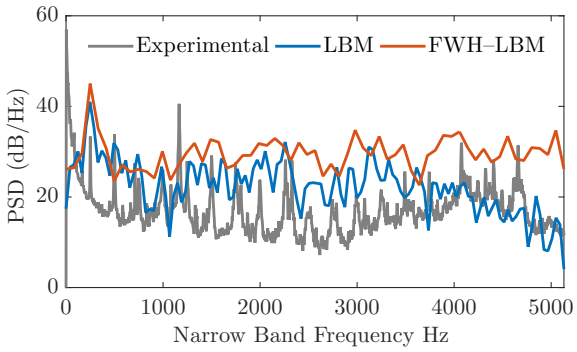

Figure 17. Acoustic power spectral density (PSD) from measurements and numerical predictions from LBM simulation at one microphone position in the rotor plane.

to identify a hierarchy in the sources of noise. The FWH equation is generally written in a way that links mathematical terms with physical meaning. The corresponding acoustic pressure for each of the terms in the FWH equation in the form of a directivity pattern centered on the rotor is shown in figure 18 for the perpendicular plane of rotation. The directivity contours give insight into the acoustic radiation pattern around the MAV rotor. The total acoustic radiation seems mostly equal in every direction, although the acoustic intensity seems higher in the downwards direction as can be expected. The most striking feature of the directivity patterns is the monopole term being dominant. It is consistant with observation from figure 17 where BPF is overestimated and mainly comes from the steady loading which the monopole term account for. However, loading noise, represented by the dipole terms, is generally considered as dominant in low–Reynolds number fan [29] due to unsteady loading. Analysis of the broadband noise models also suggests that dipole terms are expected to be dominant for interaction noise, believed by the authors to be the main noise source in this configuration, is a consequence of unsteady loading. As previously observed (figure 16), interaction noise in MAV rotors is a broadband, high–frequency component of the acoustic spectrum and it might not be resolved yet by the FWH tool addressed in this contribution, as a result of the high frequency resolution available at this early stage. As a consequence, the dipole terms of the FWH equation might be underpredicted.

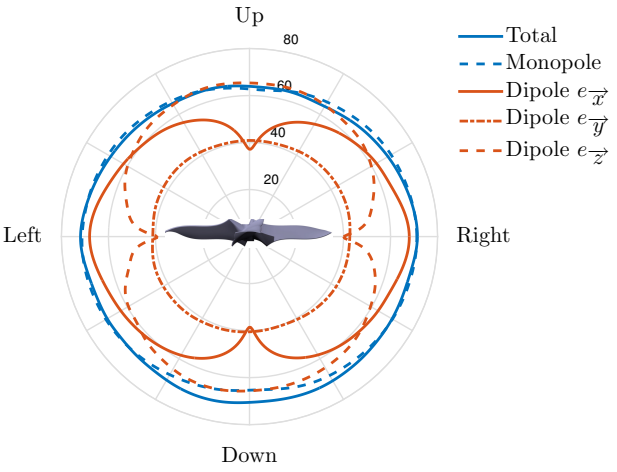

Figure 18. Directivity contour perpendicular to the plane of rotation at $r = 1$ m away from the rotor. Corresponding acoustic pressure from multipole terms in the FWH equation [25]. Levels in dB. Rotor is not at scale.

4. DISCUSSION

The optimization has proven its effectiveness to reduce the noise produced by MAV rotors in hover and increase endurance. A reduction of 8 dB(A) in the acoustic power is obtained and experimentally observed from a protocol suitable for non–treated rooms. High levels of noise reduction are expected in the future using the tools presented herein. However, the optimization presented in this contribution is first of all an aerodynamic optimization. Acoustic models in the optimization tool estimate noise levels from steady loading but experiment and numerical simulations suggest that unsteady aerodynamics induces most of the noise. In such a context, reducing the rotational speed or optimizing the aerodynamic efficiency will lead to lower noise levels as rotational speed is the driving parameter for the involved noise mechanisms. Another source of noise is under investigation with implementation of vortex shedding broadband noise model [12]. The dominant source of noise is found to be produced by the interaction between turbulence and leading edge. The turbulence impinging the leading edge is relatively homogeneous, and if most of the noise is produced in the leading edge region, a specific design should be able to significantly reduce acoustic radiation by destroying homogeneous turbulence or by allowing phase cancellation of the acoustic waves resulting from the scattering of turbulence wavelength by the leading edge.

ACKNOWLEDGMENTS

This research is supported by Direction Générale de l'Armement (DGA) from the French Ministry of Defense. The authors thank Rémy Chanton from the technical team for the set–up of the aerodynamic balance.

REFERENCES

[1] A. Pagano, M. Barbarino, D. Casalino, and L. Federico. Tonal and broadband noise calculations for aeroacoustic optimization of propeller blades in a pusher configuration. *Journal of Aircraft*, 47(3):835–848, 2010.

[2] S. Pednekar, D. Ramaswamy, and R. Mohan. Helicopter rotor noise optimization. In *5th Asian-Australian Rotorcraft Forum*, 2016.

[3] C. F. Wisniewski, A. R. Byerley, W. H. Heiser, K. W. Van Treuren, and W. R. Liller. Designing small propellers for optimum efficiency and low noise footprint. In *33rd AIAA Applied Aerodynamics Conference*, number AIAA-2015-2267, 2015.

[4] N. S. Zawodny, D. Douglas Boyd Jr, and C. L. Burley. Acoustic characterization and prediction of representative, small–scale rotary–wing unmanned aircraft system components. In *72nd AHS Annual Forum*, 2016.

[5] R. Serré, V. Chapin, J. M. Moschetta, and H. Fournier. Reducing the noise of micro–air vehicles in hover. In *International Micro Aerial Vehicle Conference*, 2017.

[6] H. Winarto. BEMT algorithm for the prediction of the performance of arbitrary propellers. Melbourne: The Sir lawrence Wackett Centre for Aerospace Design Technology, Royal Melbourne Institute of Technology, 2004.

[7] C. A. Lyon, A. P. Broeren, P. Giguère, A. Gopalarathnam, and M. S. Selig. Summary of low–speed airfoil data volume 3. SoarTech Publications, Virginia Beach, VA, 1998.

[8] J. Morgado, R. Vizinho, M. A. R. Silvestre, and J. C. Páscoa. XFOIL *vs* CFD performance predictions for high light low Reynolds number airfoils. *Aerospace Science and Technology*, 52:207–214, 2016.

[9] M. Drela and M. B. Giles. Viscous–inviscid analysis of transonic and low Reynolds number airfoils. *AIAA Journal*, 25(10):1347–1355, 1987.

[10] M. E. Goldstein. *Aeroacoustics*. McGraw-Hill Book Co., 1976.

[11] J. E. Ffowcs Williams and D. L. Hawkings. Sound generation by turbulence and surfaces in arbitrary motion. *Philosophical Transactions of the Royal Society of London*, 264(1151):321–342, 1969.

[12] M. Roger and S. Moreau. Extensions and limitations of analytical airfoil broadband noise models. *International Journal of Aeroacoustics*, 9(3):273–305, 2010.

[13] F. Farassat and G. P. Succi. A review of propeller discrete frequency noise prediction technology with emphasis on two current methods for time domain calculations. *Journal of Sound and Vibration*, 71(3):399–419, 1980.

[14] G. Sinibaldi and L. Marino. Experimental analysis on the noise of propellers for small UAV. *Applied Acoustics*, 74:79–88, 2013.

[15] Y. Rozenberg, M. Roger, and S. Moreau. Rotating blade trailing–edge noise : experimental validation of analytical model. *AIAA Journal*, 48(5):951–962, 2010.

[16] J. G. Leishman. *Principles of Helicopter Aerodynamics*. Cambridge University Press, 2002.

[17] N. Kloet, S. Watkins, X. Wang, S. Prudden, R. Clothier, and J. Palmer. Drone on: a preliminary investigation of the acoustic impact of unmanned aircraft systems (UAS). In *24th International Congress on Sound and Vibration*, 2017.

[18] S. Marié and P. Sagaut. Comparison between Lattice Boltzmann Method and Navier–Stokes high order schemes for computational aeroacoustics. *Journal of Computational Physics*, 228(4):1056–1070, 2009.

[19] P. A. Durbin and B. A. Pettersson Reif. *Statistical theory and modeling for turbulent flows*. John Wiley and Sons, Inc., 2nd edition, 2011.

[20] Y. Rozenberg. *Modélisation analytique du bruit aérodynamique à large bande des machines tournantes : utilisation de calculs moyennés de mécanique des fluides*. PhD thesis, École Centrale de Lyon, 2007.

[21] V. Blandeau. *Aerodynamic broadband noise from contra–rotating open rotors*. PhD thesis, University of Southampton, 2011.

[22] Y. N. Kim and A. R. George. Trailing–edge noise from hovering rotors. *AIAA Journal*, 20(9):1167–1174, 1982.

[23] R. K. Amiet. Acoustic radiation from an airfoil in a turbulent stream. *Journal of Sound and Vibration*, 41(4):407–420, 1975.

[24] T. Fukano, Y. Kodama, and Y. Senoo. Noise generated by low pressure axial flow fans, I: modeling of the turbulent noise. *Journal of Sound and Vibration*, 50(1):63–74, 1977.

[25] X. Gloerfelt, C. Bailly, and D. Juvé. Direct computation of the noise radiated by a subsonic cavity flow and application of integral methods. *Journal of Sound and Vibration*, 266:119–146, 2003.

[26] G. A. Brès, F. Pérot, and D. Freed. A Ffowcs Williams–Hawking solver for Lattice–Boltzmann based computation aeroacoustics. In *16th AIAA/CEAS Aeroacoustics Conference*, number AIAA-2010-3711, 2010.

[27] L. V. Lopes, D. Douglas Boyd Jr, D. M. Nark, and K. E. Wiedemann. Identification of spurious signals from permeable Ffowcs Williams and Hawkings surfaces. In *73nd AHS Annual Forum*, 2017.

[28] D. P. Lockard. An efficient, two–dimensional implementation of the Ffowcs Williams and Hawkings equation. *Journal of Sound and Vibration*, 229(4):897–911, 2000.

[29] S. Magne, S. Moreau, and A. Berry. Subharmonic tonal noise from backflow vortices radiated by a low–speed ring fan in uniform inlet flow. *Journal of the Acoustical Society of America*, 137(1):228–237, 2015.